Performance of spatial vs. temporal phase shifting in ESPI

Jan Burke, Heinz Helmers*

Carl von Ossietzky Universität Oldenburg, FB 8 Physik, PF 2503, D-26111 Oldenburg

ABSTRACT

We compare quantitative phase-measuring techniques in ESPI, using temporal and spatial phase shifting (TPS and SPS). The latter is less susceptible to time-dependent disturbances but inherently yields higher noise in the results due to the spatial intensity and phase variations of the object speckle field. Moreover, the necessity of larger speckles limits the light efficiency in SPS. Based on an evaluation of phase errors in sawtooth images, we compare both of the methods quantitatively in various ESPI configurations. By varying quantities like speckle size and shape and sawtooth fringe density, we find out characteristic behaviours of the methods. Some strategies to optimise the accuracy of the SPS method are explored to estimate how competitive SPS can be in ESPI systems.

Keywords: ESPI, temporal phase shifting, spatial phase shifting, phase errors, beam ratio, Fourier transform method

1. INTRODUCTION

The application of the phase shifting technique has made ESPI a versatile quantitative tool in non-destructive testing, with numerous scientific and industrial applications. A drawback of the widespread temporal phase-shifting method (TPS), where the phase-shifted data are acquired in a temporal sequence of camera frames, is the susceptibility to external disturbances like vibrations, turbulences in the optical medium, or rapid motion of the test object itself. There have been attempts to minimise the influence of time-dependent parameter fluctuations in TPS[1,2]; there is however another very simple way to get rid of problems with instability. This method is known as spatial phase shifting (SPS), where the data required are recorded simultaneously, either by several cameras with the appropriate static phase shift for each of the images[3] or encoded by a carrier fringe pattern on one video target[4,5]. Particularly the latter approach is quite attractive thanks to its simple implementation that needs neither costly optics nor electronics nor moving parts. Fig. 1 shows the principle.

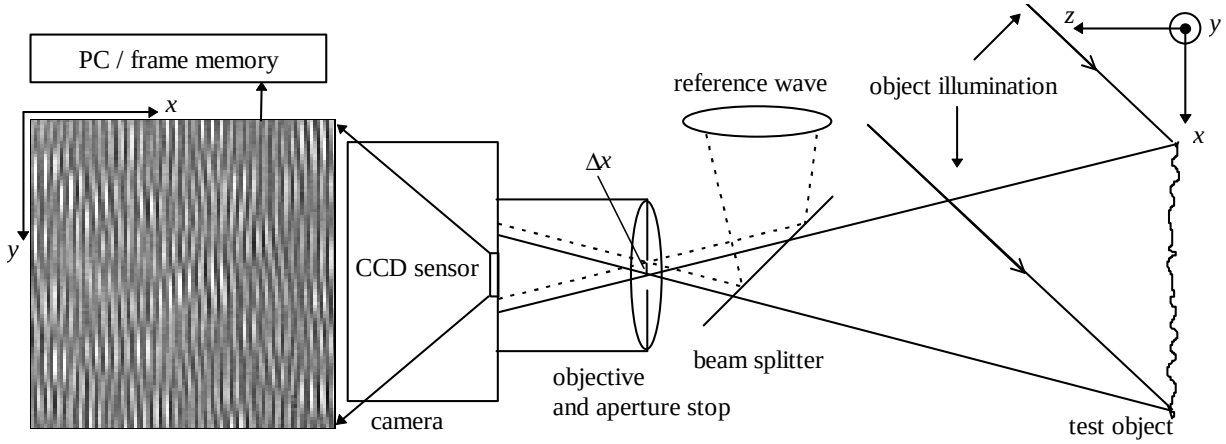

Fig. 1: Principle sketch of an ESPI system with spatial phase shifting. Image on left side: magnified part of actual SPS interferogram.

The set-up resembles a quite conventional ESPI configuration, except for one modification: the reference wave's source point is given a slight lateral offset Δx from the centre of the aperture, which generates a quasi-linear phase ramp $\alpha(x)$ on the sensor[5]. Thus, provided the speckle size is appropriately increased, the phase-shifted data are arranged on adjacent sensor pixels. This facilitates phase retrieval out of one frame, so that even very fast transients can be frozen and/or tracked. Unfortunately, these advantages are accompanied by some restrictions in ESPI. Let us briefly review why. Phase-shifting formulae are derived from a set of interferometric equations that read for TPS:

* heinz.helmers@uni-oldenburg.de; http://www.uni-oldenburg.de/physik/Docs/holo; phone: +49-441-798-3512, fax: -3576

$$I_i\left(x,y,t_i\right)=I_0\left(x,y\right)\left[1+\gamma\left(x,y\right)\cdot\cos\left(\varphi_s\left(x,y\right)+\varphi_o\left(x,y,t_i\right)+\alpha_i\left(t_i\right)\right)\right], \tag{1}$$

and for SPS:

$$I_i\left(x_i,y\right)=I_0\left(x_i,y\right)\left[1+\gamma\left(x_i,y\right)\cdot\cos\left(\varphi_s\left(x_i,y\right)+\varphi_o\left(x_i,y\right)+\alpha_i\left(x_i\right)\right)\right]. \tag{2}$$

The I_i are the measured intensities in the ith phase sample (frame or pixel), I_0 is the bias intensity, γ the modulation or contrast, φ_s, speckle phase, φ_o, object phase to be found, and α_i, additional phase shift in the ith phase sample. Usually φ_s cancels out by subtraction of two phase maps representing two object states, and we have three unknowns, I_0, γ, and φ_o, which is why this approach requires three or more I_i. In solving for φ_o, one relies on the constancy of I_0, γ, φ_s and φ_o throughout the set of data. Problems with TPS arise from time-dependent fluctuations in φ_o, while the other unknowns may be assumed constant for each pixel (x,y) and hence play no role in the pixelwise phase calculation. In SPS however, the I_i come from adjacent sensor pixels (x_i,y), and the I_0, γ, φ_s are not at all constant, since the object wave is a speckle field, known to consist of spatial phase and intensity variations.

While TPS measurements are even possible with unresolved speckles[6] and a wide open aperture, SPS tends to make uneconomic use of the object light: the mean speckle size in the direction of the phase shift must be about three pixels to assure sufficient spatial correlation in the $\varphi_s(x_i,y)$ for phase shifting to make sense. Even then, phase retrieval algorithms that can compensate for intensity and/or phase variations, as known from TPS[7], are highly desirable and have been implemented in simple versions with three or four phase samples[8]. The larger speckle size is also associated with a lower spatial resolution. So, while very good TPS measurements are possible when φ_o is reasonably stable, the measurement accuracy achieved by SPS can be expected to be somewhat inferior. This brings up the question whether the theoretical disadvantages of SPS constitute any relevant practical shortcomings, and if so, whether SPS can be improved to equal the accuracy of TPS.

The present study is an attempt to settle this question by providing quantitative performance data in terms of the rms phase error in unfiltered sawtooth images. To obtain comparable data, the TPS and SPS measurements were done with the very same laboratory interferometer. This environment is perfectly suitable to apply both TPS and SPS under optimal conditions. For all except the Fourier-technique phase calculations, we use a simple standard 3-bucket 120° algorithm,

$$\varphi=\arctan\frac{\sqrt{3}(I_1-I_3)}{2I_2-I_1-I_3}, \tag{3}$$

and test the influence of various experimental parameters on the rms phase error in the sawtooth phase maps obtained.

2. EXPERIMENTAL SET-UP

Our goal is to collect displacement data by TPS and SPS from out-of-plane and in-plane displacements with the respective interferometer configurations. The results that we wish to compare must of course be obtained under the same experimental conditions, which is easiest to achieve with the same set-up. Therefore we designed a speckle interferometer capable of TPS and SPS with only one minor change. Fig. 2 depicts the arrangement. The light from a 50-mW HeNe laser is split by BS1; for a compact set-up, BS2 guides the reference light path close to the one of the object. The object light is expanded by MO1 and collimated by a large lens of 250 mm focal length, L1, which serves to obtain a uniform field of sensitivity. M3 directs the light onto the object at an angle of $\simeq 7.5°$ to the surface normal, which gives a quasi-out-of-plane set-up. The light spot on the object has a diameter of some 10 cm, of which only 28.5x21.5 mm² are imaged onto the CCD sensor by L2 with a magnification of $M = 0.26$. The object is an aluminium plate sprayed matt white that can be tilted about all three spatial axes. By the piezo-driven mirror M2, we have a possibility to use TPS. The polarisation filter PF attenuates the reference light to the extent required. By MO2 the reference wave is coupled into a fibre. The fibre is held in place by a bent syringe cannula and guides the reference light onto the sensor. As the aperture A, we used laser-cut aluminium plates with circular or elliptic holes. The distance Δx of the fibre end relative to the aperture's centre determines the spatial phase shift $\alpha_x(x)$. It is set to zero ($\Delta x = 0$) for the TPS measurements and to $\alpha_x(x)$=120°/column for SPS and calibrated by the Fourier method[5] for either setting.

For TPS, a control bit from the PC triggers a sawtooth waveform generator that drives the piezo via an HV amplifier. The voltage ramp is chosen so as to generate a nominal phase shift of $\alpha_t(t)$=120°/frame. While the sequence is in progress, four consecutive camera frames are stored, of which the first and the last one are subtracted. If their mean brightness difference

exceeds a certain threshold, an external mechanical or thermal disturbance is present, the frames are discarded and the sequence is repeated. Otherwise the phase shift of all recorded frames was assumed to be correct; additional tests confirmed it to be accurate within ± 5%. This is the well-known „dark frame“ calibration method[9]. Note here that both of the techniques are implemented as integrating-bucket versions.

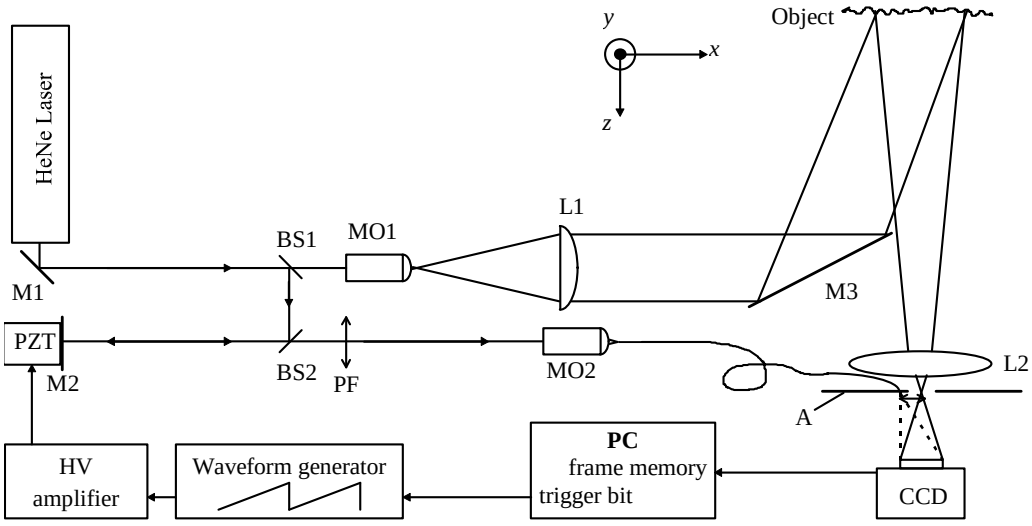

Fig. 2: Optical set-up used for TPS and SPS. Abbreviations: M, mirrors, BS, beam splitters, L, lenses, MO, microscope objectives, PF, polarisation filter, PZT, piezo actuator, A, aperture.

For the other configurations, changes of rather different extent are necessary that are not drawn here for the sake of clarity. The mixed in-plane/out-of-plane configurations (henceforth referred to by this term) are realised by additional mirrors close beside and above the object, allowing displacement measurement of the *x* or *y* co-ordinate, respectively. They are illuminated one at a time by adjusting M3 appropriately to direct the light onto the object at oblique incidence. Their positions are chosen to give a sensitivity vector inclined by 26.6° to the surface normal, so that the in-plane sensitivity is half the out-of-plane sensitivity. For the pure in-plane TPS experiments, the illumination arrangement was a largely different one[10]; however the imaging geometry could be maintained. The pure in-plane measurement by SPS requires a completely different set-up[11] and has little in common with the other experiments.

3. DATA EVALUATION

Often when accuracies of ESPI are given, we encounter rough estimates of, say, $\lambda/10$ without and $\lambda/30$ with phase shifting; it is seldom stated to what stage of data processing the data refer. Hence we need a tool to obtain more precise values. To standardise and simplify our results, we omit any kind of low-pass filtering or unwrapping of the sawtooth images and work with raw data. We handle these by a long-known and widespread fitting algorithm called the “downhill simplex method“[12] to calculate the rms displacement error from sawtooth images. The quantity the fitting routine actually uses are the pixels´ grey values; these are however easily mapped onto phase and displacement by knowledge of the interferometer geometry. In its present version, the algorithm works on images with straight and equispaced fringes only. This is however sufficient for our purpose, since we can generate such fringe patterns by tilt or rotation of the test object for out-of-plane and in-plane configurations, respectively.

The idea of data fitting is as follows. A sawtooth image with straight and equispaced fringes is defined by three parameters only: (i) number of fringes per sensor width (1024 pixels) in x-direction, $\boldsymbol{N}_x$; (ii) number of fringes per sensor height (1024 pixels) in y-direction, $\boldsymbol{N}_y$; and (iii) phase offset φ_0 at some arbitrary point (in fact, the upper left corner that is interpreted as (0,0) by computer graphics, cf. Fig. 1). This constitutes a three-dimensional parameter space. The ideal data set is assumed to be a noise-free sawtooth function in *x* and/or *y*, from which the real data deviate more or less. For a given input image, the fitting algorithm takes the initial guess of the parameter set ($\boldsymbol{N}_x$, $\boldsymbol{N}_y$, φ_0), generates a noise-free fringe system from it and calculates its rms deviation from the input image. As the rms is minimised, the point ($\boldsymbol{N}_x$, $\boldsymbol{N}_y$, φ_0) is moved through the $\mathbb{R}^3$, and its final location defines the parameters of the best-matching ideal fringe system. The remaining errors eventually

include large- and small-scale, random and deterministic errors and allow a quantitative statement about a measurement´s accuracy. Fig. 3 gives an example of the algorithm at work, just executing the last iteration.

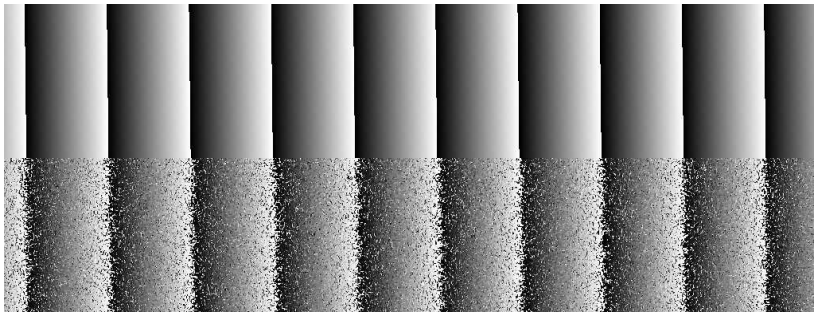

Fig. 3: Downhill simplex algorithm during last iteration; upper half, best-fit fringe system, laid over real data still visible in lower half.

This fitting method can be easily extended to greater dimensionality. If, for instance, a cosine profile is to be evaluated, two degrees of freedom, bias intensity and fringe modulation, are added and the algorithm can determine the fringe visibility in $\mathbb{R}^5$. More complicated fringe structures could also be treated. In any case, the output is an average over the whole image and therefore statistically very reliable. The minimum possible rms error (digitisation alone) is 0.29 grey values, and as can be expected, the maximum error (trying to find a fringe system in random noise, e.g. a speckle phase map) amounts to 73.9 grey values. This is the rms of a uniform distribution within the range [-128,128[, corresponding to phase in the range [-π,π[. The error is confined to [-π,π[because phase errors larger than π, i.e. of ±(π+c), 0<c<π, are wrapped back onto ∓(π–c) due to the cyclic nature of the phase.

4. PARAMETER OPTIMISATION

Although the best intensity ratio of reference and object wave (defined as beam ratio) has been thoroughly investigated[13,14], it has also been stated that the minimum modulation depth can be set quite low, i.e. at some 8 grey levels[15]. Consequently, phase shifting in ESPI yields reasonable results for quite a large range of the beam ratio. In what concerns TPS, we can expect the errors to remain approximately constant in the high-modulation range. With growing intensity of the reference wave, the modulation drops and electronic noise and digitisation errors gradually gain the upper hand over the signal. For SPS however, we encounter a different situation: increasing the reference intensity can diminish the errors from intensity variations in the object speckles significantly. To understand why this is so, we first give a short intuitive reasoning. The measured (superscript *m*) intensities at three adjacent pixels are given by

$$I_i^m = O_i + R + 2\cdot\sqrt{O_i\cdot R}\cdot\cos\left(\varphi_s + i\cdot\frac{2\pi}{3}\right),\quad i\in[1,2,3], \tag{4}$$

where O_i is the object irradiance at pixel x_i and the reference intensity R is assumed spatially constant. We have omitted all spatial dependencies that are of no concern in this discussion. The range of i is restricted here for simplicity; in practice, the pixel triplet moves sequentially from (1,2,3) to (N-2, N-1, N), where N is the column count of the CCD array. Clearly, it is the variation in the O_i that gives rise to bias and contrast mismatch in the pixel triplet. If we assume O_1=O_2=O_3, the ideal expected (superscript *e*) intensities would be

$$I_i^e = O_2 + R + 2\sqrt{O_2\cdot R}\cdot\cos\left(\varphi_s + i\cdot\frac{2\pi}{3}\right). \tag{5}$$

The difference between measured and expected intensities is

$$\Delta I_i = I_i^e - I_i^m, \tag{6}$$

and we find the relative error of the intensities to be

$$\frac{\Delta I_i}{I_i^e} = \frac{O_2 - O_i + 2\sqrt{R}\cdot\left(\sqrt{O_2}-\sqrt{O_i}\right)\cdot\cos\left(\varphi_s + i\cdot\frac{2\pi}{3}\right)}{O_2 + R + 2\cdot\sqrt{R}\sqrt{O_2}\cdot\cos\left(\varphi_s + i\cdot\frac{2\pi}{3}\right)},\ i\in[1,3], \tag{7}$$

which approaches zero as $R\to\infty$.

After this intuitive consideration, let us turn towards a more analytical but still simplified treatment. The quantity of interest is the rms *phase* error caused by the ΔI_i. The propagation of statistical intensity errors into the calculated phase is described by Eq. (12) in Ref. 5, and in this context we can write

$$\sigma_{\bar{\varphi}} = \frac{\sigma_{O_2,O_j} + \sigma_n}{2 \cdot \sqrt{O_2 \cdot R}} \cdot \sqrt{\frac{8}{3}}, \quad j \in [1,3], \tag{8}$$

with $\sigma_{\bar{\varphi}}$ denoting the standard deviation of the calculated phase averaged over all φ, $\sigma_{O2,Oj}$ denoting the standard deviation of the object intensity at adjacent pixels, and σ_n modelling the electronic noise (2.5 grey values rms is realistic here). Now, $\sigma_{O2,Oj}$ depends on the degree of coherence[16], $\mu(x_2,x_j)$, of the points (x_2,x_1) or (x_2,x_3) apart by 1/3 speckle diameter. For a circular aperture, we find $\mu(x_2,x_j) \simeq 0.81$. Moreover, $\sigma_{O2,Oj}$ is conditioned on O_2, which relationship is analytically known[17]. We can generalise Eq. (8) in Ref. 17 to read

$$\left\langle \sigma_{O_2,O_j} \right\rangle = \sqrt{\left[\langle O \rangle (1-\mu^2)\right]^2 + 2\langle O \rangle \mu^2 (1-\mu^2) \langle O \rangle}\,, \tag{9}$$

where $\langle O \rangle$ is the average intensity of the speckle field. The average (9) is inserted into (8) and has to be appropriately re-scaled like the modulation $2 \cdot \sqrt{O_2 \cdot R}$ as we let $R \to \infty$, for the measurement is confined to 256 intensity units. (In practice we reduce the video signal amplification as R grows; consequently the modulation and speckle intensity readouts drop.)

These considerations account for intensity errors only and neglect the phase structure of the speckle field completely so that the predicted error will be too small. Therefore we have shifted the calculated curve in Fig. 4 upwards by 0.05 λ to see better whether the error depends on the beam ratio in the expected way. The experimental results shown in Fig. 4 were obtained from sawtooth images with N_x=10 and 3 pixels/speckle for both SPS and TPS. The electronic system used for image pick-up was a full-frame camera (ADIMEC MX12P) with analogue, pixel-clocked output, attached to a Data Translation DT3852 frame grabber with 8-bit A/D conversion.

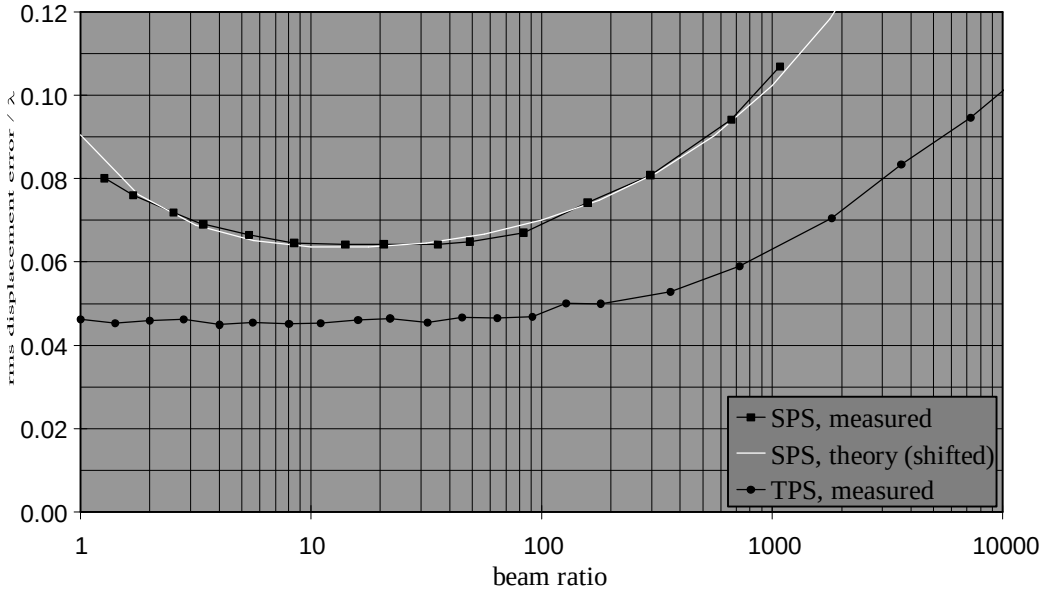

Fig. 4: rms phase errors measured with SPS and TPS, and calculated for SPS, at different beam ratios.

From Fig. 4 we see that TPS measurements function well from a beam ratio of 1:1 on, and only start to deteriorate when we drive it to 100:1, where the object intensity in the speckle field is already weaker than the electronic noise. For SPS, the rms displacement error first decreases as the reference wave gets stronger, and has its minimum between 10:1 and 30:1. With fading data modulation, the influence of electronic noise grows and so does the error.

Besides the variation of the beam ratio, we have described another possibility of reducing errors by incorporating the individual speckle intensities into a modified phase calculation formula[5,8]. But we found that its best performance is almost reached in the minimum error region shown here, and therefore chose a beam ratio of 10:1 for the experiments, at which settings both of the methods work almost optimally.

5. COMPARISON OF TPS AND SPS

5.1 Zero-displacement measurements

Of the results of phase measurements that will be presented here, those with zero displacement gradient are the most general ones, since they do not depend on the specific assembly's parameters but should be comparable for any set-up with only the speckle size as the relevant quantity. The way to obtain such measurements is to leave the object untouched and to compare two nominally identical object states, differing only by a controlled or random global phase offset $\Delta\varphi$. Unfortunately, in SPS the value of $\Delta\varphi$ influences the rms phase error strongly due to the ample intensity and phase gradients in the object speckle field. An example of this behaviour is shown for three different speckle sizes and 120 measurements for each of them in Fig. 5.

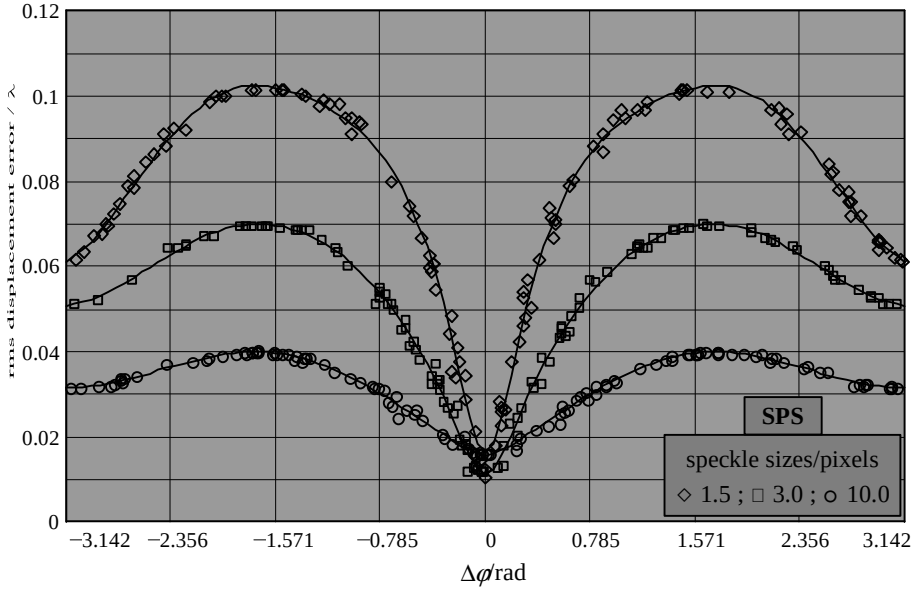

Fig. 5: Dependency of the rms displacement error as determined by SPS on the global phase offset for three different speckle sizes.

When set in relation to previous results from TPS[9,18], the qualitative appearance of the graphs suggests that the underlying phenomenon could mainly a linear miscalibration of phase shift: when we subtract one phase map from another, the errors thus produced theoretically cancel at phase differences of 0 and π, and add up in between these values. If we consider the phase gradients in speckle fields[19], leading to substantial local detuning of the carrier fringes, this explanation of Fig. 5 seems reasonable. The lowest phase error occurs at global phase shifts near zero where, except for electronic noise, both interferograms simply look the same irrespective of phase shift distortions. Then with the phase offset, the error increases, depending on the speckle size. Around a phase offset of π, the error does not reach the minimum again, which tells us that there are more error sources than wrong phase shift.

We have calculated the average zero-displacement error from fitting suitable functions (given in the figure as well) to the data points and determining their mean values, since the distribution of the measured values themselves would not be uniform enough to obtain the average directly. The values finally obtained constitute the entries for "0 fringes/1024 pixels" appearing in the following plots. The error profiles of Fig. 5 also occur within displacement fringes (in which $\Delta\varphi$ progresses deterministically from $-\pi$ to π), so that the rms phase error that we assign to sawtooth images is in itself an average over all $\Delta\varphi$. Fortunately though, we find the least error near the most critical regions of the sawtooth images, namely the 2π jump boundaries that are so crucial to the less sophisticated unwrapping algorithms.

With TPS, none of these detours is necessary; the phase error does not depend on the global phase offset, provided the phase shift is calibrated exactly enough. Consequently, one measurement with zero displacement gradient is sufficient to determine the corresponding error. Furthermore, the displacement error is uniformly distributed in sawtooth fringes from TPS, and there is no such thing as an error fringe profile in this case.

5.2. Out-of-plane configuration

In order to come to a statement about the fringe quality delivered by the methods, we first repeated a series of out-of-plane tilt measurements with varying speckle sizes. Tilts about the *y*-axis, producing 5, 10, 20, 30, and 40 vertical fringes per 1024 pixels, were adjusted in the SPS and TPS configurations for each speckle size. Appropriate combinations of the measured speckle phase maps enabled the error values for higher fringe counts to be found. The results are displayed in Fig. 6.

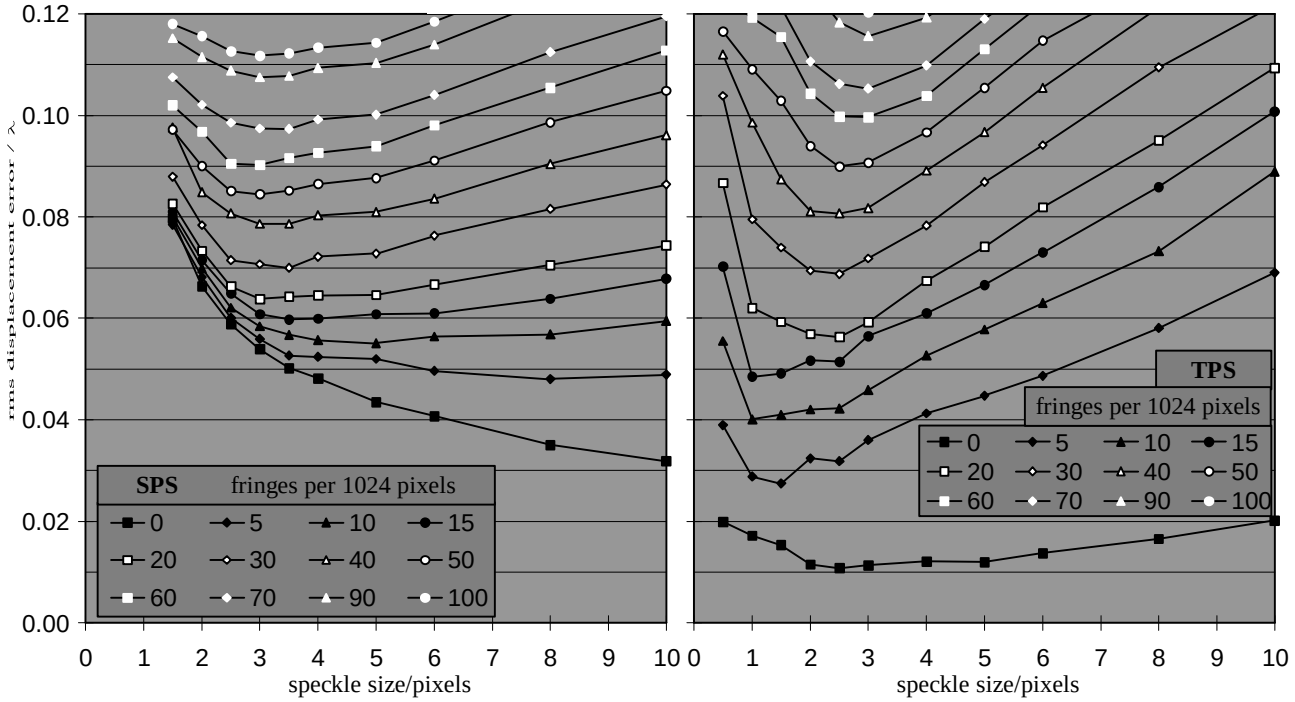

Fig. 6: rms displacement error of SPS (left) and TPS (right) as a function of speckle size. The parameter for each curve is the number of fringes per 1024 pixels, as indicated in the legend boxes.

The SPS experiments confirm a speckle size of about 3 pixels to be most suitable for SPS. Small tilts can be measured with very large speckles; denser fringes however are badly resolved. With too small speckles, i.e. a mean speckle size below some 2.5 pixels, the phase error increases steeply, especially for low fringe densities. From this we see that the SPS method is not very tolerant against low spatial coherence of the data points. In the TPS experiments, a speckle size around 1 pixel turns out to yield the lowest error for lower fringe densities; yet at larger tilts, we obtain better measurements with larger speckles. From this it gets clear that we encounter two effects here: (i), speckle field *decorrelation*, which progresses faster for small apertures (large speckles) as we increase the tilt; (ii), speckle pattern *displacement* due to object tilt, which leads to an increasing pixel position mismatch. But the same speckle displacement introduces less noise when the speckles are larger, although the pattern in itself decorrelates faster. Generally, TPS is significantly more accurate at low fringe densities; however its advantage fades quickly with increasing displacement.

5.3 In-plane configurations

When carrying out in-plane displacement measurements by SPS and assessing its performance, the reference is the ingenious symmetrical pure-in-plane TPS configuration[10] with its excellent sensitivity. A pure-in-plane SPS configuration using a double aperture has been established[11], and we will investigate its merits, but it also seems worthwhile to modify the set-up of Fig. 2 for more oblique object illumination (as described in Section 2) and to gain in-plane sensitivity in this way, since this arrangement is by far easier to handle. The sequence of experiments described consists of object rotations about the z axis (which also generates straight and equidistant fringes, only for the in-plane displacement now), again with speckle sizes varying from 10 to 0.5 pixels. For the purely in-plane sensitive configurations, only the *x*-displacement was measured. As the mixed-sensitivity set-up for SPS is easy to change, we recorded *x*- and *y*-displacements with it, which showed the same behaviour. Fig. 7 gives an overview of the performance of the different methods.

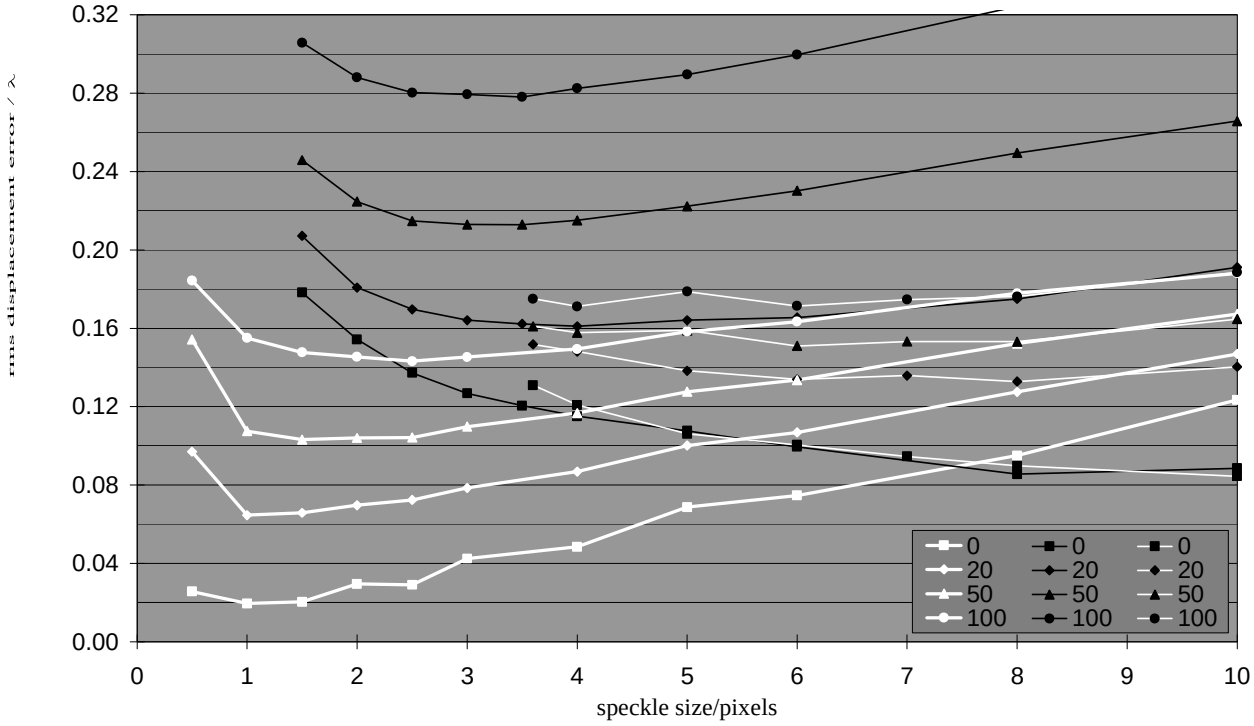

Fig. 7: rms displacement errors for in-plane measurements with pure in-plane symmetrical set-up: TPS (all white, bold lines) and SPS (white lines, black symbols), and SPS with mixed-sensitivity set-up (all black). Note the augmented ordinate scale.

For the TPS measurement, the phase error is quite similar to that from the TPS out-of-plane configuration. The pure-in-plane SPS set-up was arranged to give the same sensitivity (1.4 sawtooth fringes per wavelength of displacement) as the pure-in-plane TPS configuration; however the speckle size is restricted to 3 pixels or larger, because the diameter of the two apertures needed (determining the speckle size) cannot exceed their distance (determining the spatial phase shift). The beam ratio for the (speckled-reference) pure-in-plane set-ups is of course unity, which makes SPS fall behind, as explained in Section 4. Besides, in the SPS system we generate the carrier frequency by oblique superposition of two speckle patterns, which results in an even greater carrier fringe distortion than in the SPS out-of-plane configuration. Consequently, a speckle size of not 3 but 6 pixels turns out to give the best results. Still, the errors thus produced are considerably larger than those of TPS; moreover the apertures have to be very small to generate 6-pixel speckles, so that the issue of light economy is very critical here.

The mixed-sensitivity SPS configuration does produce smaller *phase* errors in the sawtooth image; but due to the lower in-plane sensitivity (0.8 sawtooth fringes per wavelength of displacement), the conversion to *displacement* yields a higher error. Also, it takes about twice the displacement in the mixed configuration to generate the same fringe density, which is why the error rises so rapidly for higher fringe counts: it comes mainly from speckle displacement. Nevertheless it may prove better to use the mixed-sensitivity set-up: since displacement data are eventually retrieved after unwrapping, the raw data must have low *phase* error to make unwrapping easy. On the whole, the results presented here show an advantage for TPS when in-plane displacement measurements are concerned. For moderate fringe densities, an rms error of $\lambda/20$ is realistic, while both of the SPS approaches yield $\lambda/6$ to $\lambda/7$.

6. IMPROVEMENTS ON SPS

In this chapter we switch back to the out-of-plane configuration to test two approaches of error reduction in SPS.

6.1 Improved light efficiency by using elliptical aperture

In the present study, we did not encounter problems with collecting object light: the laser is powerful and the image field is rather small. In practical applications however, it is likely that the small aperture needed for SPS will cause problems: by

increasing the mean speckle size from one to three pixels, the available object light is reduced by almost one order of magnitude. This can be partly circumvented by enlarging the speckles only in the direction of the spatial phase shift, which is easy to achieve by using an elliptical imaging aperture. The idea is sketched in Fig. 8. Case a) shows the situation when using a circular aperture: 2/3 of the coherence area are superfluous for the phase calculation and the speckle field appears rather dark. In case b) an elliptical aperture generates elliptical speckles that are just large enough to allow for phase calculation; the speckle intensity is greater by a factor around three, indicated by the speckle spot in lighter grey.

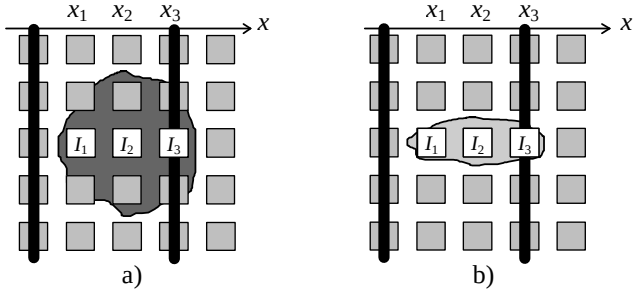

Fig. 8: Adjustment of speckle width suitable for SPS, retaining optimal light economy. Direction and spacing of the carrier fringes are indicated by the vertical black bars; small squares: sensor pixels, irregular filled shapes: mean speckle size and orientation. The I_i are given by Eq. (2). **a)**: mean speckle size 3x3 pixels; **b)** mean speckle size 3x1 pixels.

At this point the question arises what improvement the change to elliptic speckles can bring about. On the one hand, we collect more object light, which gives better fringe contrast or allows to reduce the gain of the camera amplifier; on the other hand, the non-circular speckle shape causes the measurement to become anisotropic with respect to displacement fringe orientations. Moreover, the orientation of the elliptic speckles plays a role now: since their structure is much finer in the vertical direction, the phase calculation is less tolerant against deviations of speckle slant or shape from the ideal situation depicted in Fig. 8 b).

In the experiments, we studied the behaviour of the rms phase error for an object intensity range from the first turning up of signal to the optimum where further increase of the illumination power did not improve the measurements anymore. The actual power densities on the object surface ranged from $5 \cdot 10^{-5}$ to 0.1 mW/cm². At the lowest light level the interference is just detectable whilst the speckle pattern alone is completely immersed in noise. The reference light was always adjusted so as to obtain a high average brightness of the interferograms, which reduced the noise a bit. Even so, we have high noise and low modulation due to beam ratios of more than 1000:1. The results of these measurements are plotted in Fig. 9.

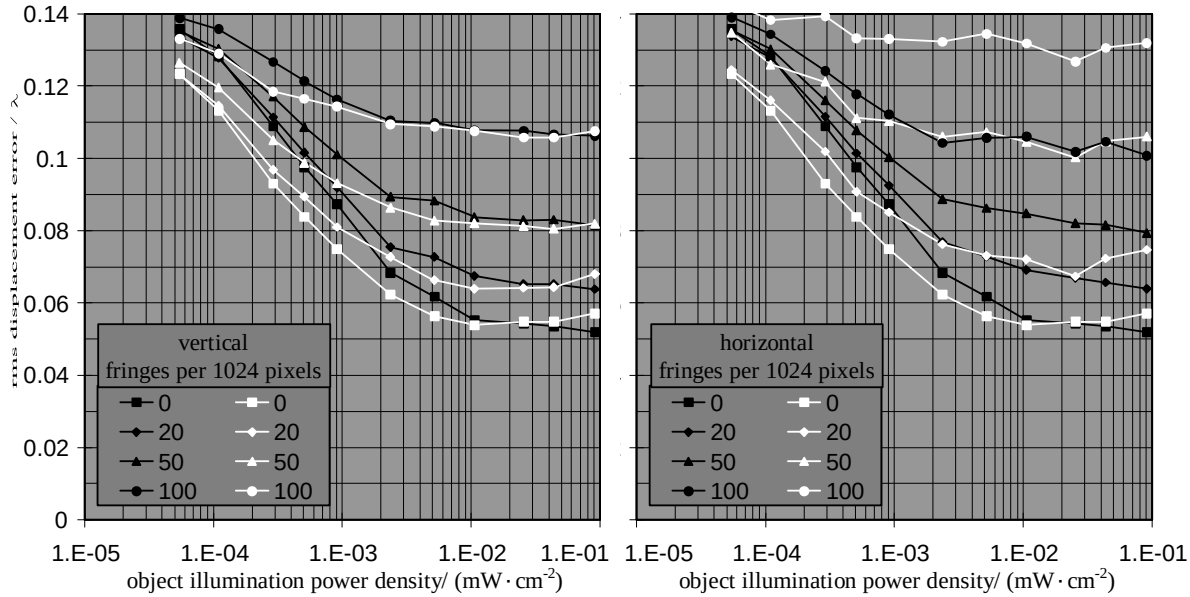

Fig. 9: Comparison of SPS measurements with circular aperture (data graphed in black) and 1:3-elliptical aperture (white) for vertical (left) and horizontal (right) sawtooth fringes.

The graphs show that at low object light levels, electronic and digitisation noise are indeed the most significant error sources: the fringe density influences the phase error only weakly. With increasing laser power however, we again get the familiar relationship of fringe density and error. Obviously, the use of an elliptical aperture does improve the measurements a bit; the error reduction amounts to as much as 15% for some regions of illumination power density.

When comparing the phase error in vertical displacement fringes against that in horizontal fringes, i.e. for displacement gradients parallel/perpendicular to the phase shift, we note that the curve arrays for the circular aperture are very similar. The elliptical aperture on the other hand causes a high error for denser horizontal fringes. Again, this comes from the speckle pattern displacement, and since now the vertical dimension of the speckles is only 1/3 of the horizontal one, the accuracy is affected more by vertical speckle displacement. This is why the initial improvement coming from the brighter speckle pattern does not last long in this case. Hence the decision for or against elliptic speckle is not a general one: it depends on the expected outcome of the experiment, as well as on the amount of light actually available. Surprisingly little power is necessary to reach the plateau of constant errors, so that there is a good amount of situations where the "primitive" set-up with a circular aperture is completely sufficient. Of course, in a TPS set-up we still get at least three times more light, which would give another 15% step of improvement. Under light conditions problematic for TPS, SPS will lead to worse SNR, but probably not fail completely.

6.2 Evaluation of SPS interferograms by the Fourier transform method

Due to the multitude of small-scale disturbances in the speckle interferogram, the spatial carrier fringe pattern is locally frequency-modulated and tilted, and even disrupted at speckle boundaries and phase singularities[19] (cf. Fig. 1). From these deviations originates a relevant broadening of the sidebands in the interferogram´s spatial frequency spectrum. This is disadvantageous for phase retrieval by means of Eq. (3), which has been shown to be a digital filter functioning correctly only within a narrow frequency band[20]. It discards or even falsifies part of the information contained in the spatial frequency sidelobe around the carrier frequency, ν_x = 1/(3 pixels), because of different frequency and phase transfer functions of numerator and denominator in Eq. (3). Decreasing the speckle size aggravates this shortcoming even more. How to deal correctly with sidelobes in this context has been demonstrated by Takeda et al.[21] with the invention of the Fourier-transform method (FTM). It has the advantage that the complete sidelobe generated by the carrier can be selected by a filter window and used for phase retrieval, i.e. while SPS works locally by a moving 3x1-pixel window, all the image information is simultaneously available to the FTM.

Although it would require sophisticated hard- and software even today to maintain the real-time capability of an SPS system with FT phase calculation, we do investigate the effect of it as a possible means of *a posteriori* data processing that still can run entirely automatically. The sizes of the sidebands to be enclosed by the frequency filter follow directly from the speckle sizes; they are half as large as the speckle halo in the frequency plane[22]. Their centres lie at ($\pm$1/(3 pixels), 0) in the frequency plane when the phase-shift is correctly adjusted. In the experiments, these theoretical parameters were met quite well. In Fig. 10, the results of the FT evaluation are compared with those from usual SPS (left) and TPS (right).

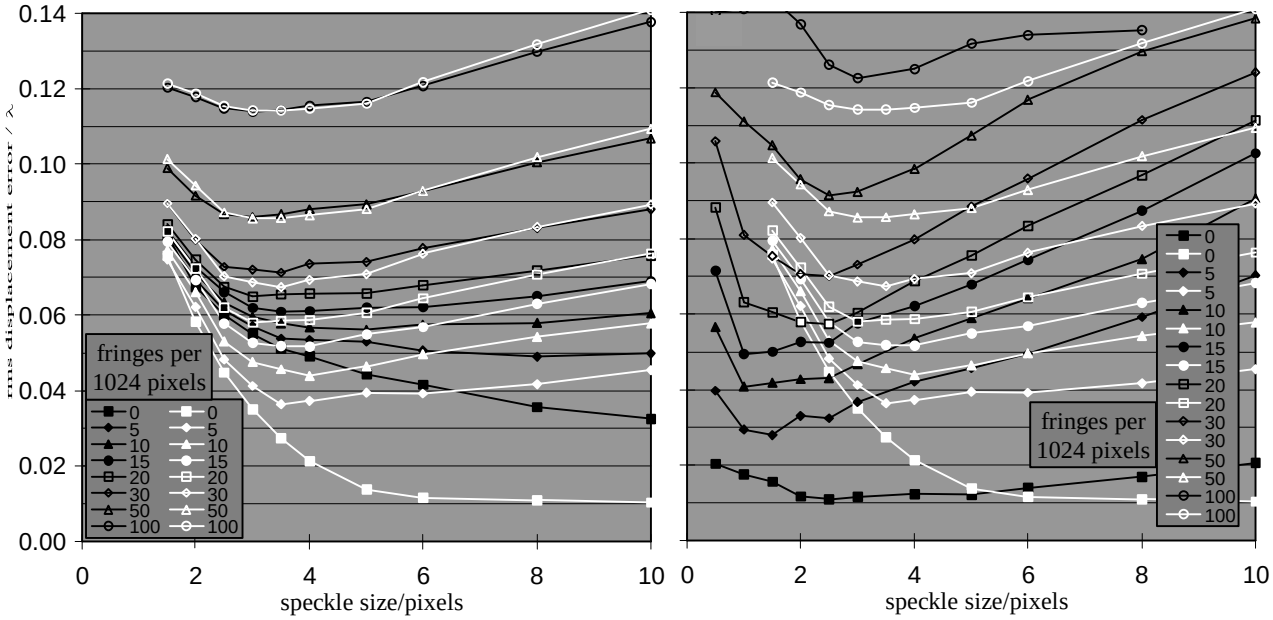

Fig. 10: Comparison of SPS (left, black) and TPS (right, black) with FTM (white, left and right identical) for vertical sawtooth fringes.

Of course, for the left plot the very same interferograms (the same as for Fig. 6) were used as input data for SPS and FTM. We see that the FTM reduces the phase error greatly for low fringe densities, while the advantage vanishes rapidly with higher fringe densities, i.e., the onset of speckle decorrelation. From a speckle size of 3 pixels downwards, there are spatial frequencies above the Nyqvist limit present in the interferograms, so that the phase reconstruction loses accuracy. Moreover the signal sidebands are no more separated from the speckle halo at small speckle sizes. Reducing the filter size does not improve the results significantly then; instead, the smaller the filter is, the coarser gets the noise structure on the sawtooth fringes, and the harder to avoid are unwrapping errors.

Comparing only the black curves in Fig. 10, we see that TPS outperforms SPS most distinctly in the region of low fringe density, as already stated in Section 5.2. This deficiency of SPS can be compensated by using the FTM. On comparing the best TPS data (around 1 pixel speckle size) with the best data from the FTM (around 3.5 pixels speckle size), we find very similar error minima from 10 fringes upwards. Hence we conclude that, provided enough object light is available, TPS can be replaced by SPS with a little extra effort: If the simple SPS evaluation yields too high an error, the images can be post-processed by the FTM and a performance very close to that of TPS can be achieved. It seems reasonable to claim an rms phase error of approximately $\lambda/20$ in raw sawtooth images for both SPS and TPS as long as out-of-plane measurements are concerned and the fringe densities do not get too high.

7. SUMMARY

There are measuring tasks in ESPI where the use of TPS is very difficult or impossible. These situations are the typical field for SPS. Its ease of use however recommends SPS more generally and also for those tasks that are accessible to TPS measurements. To assess the performance of the methods, we have compared TPS and SPS in terms of the rms error in displacement sawtooth images. To do so, a fitting routine capable of working on unfiltered images was developed. We used a multi-purpose interferometer to maintain the experimental parameters as constant as possible. The reference-to-object beam intensity ratio was set to 10:1 so as to obtain near-optimum performance for both TPS and SPS. A peculiarity of SPS, namely the inevitable dependence of the rms phase error on the phase itself, is briefly discussed. For the quasi out-of-plane configuration, we found that TPS performs better than SPS for low fringe densities and that the methods yield comparable accuracies at larger displacements. Considering pure in-plane set-ups, the situation favours TPS because of the easy-to-assemble and very sensitive pure-in-plane configuration that can hitherto not be reproduced as an equally versatile SPS version. We then address the problem of light efficiency and investigate the error reduction in SPS brought about by changing to elliptic speckles, with the result that this step should be done only when the corresponding measurement anisotropy is acceptable. Finally we investigate the help of the Fourier transform method in possible post-processing of spatially phase-shifted interferograms, and find that this facilitates an SPS performance comparable to that of TPS for out-of-

plane measurements. This study demonstrates that careful tuning of experimental parameters and appropriate use of the Fourier transform technique can help SPS in some applications to approach the performance of TPS rather closely.

ACKNOWLEDGEMENT

This work has been financially supported by the Deutsche Forschungsgemeinschaft, DFG.

REFERENCES

1. F. Mendoza Santoyo, D. Kerr, and J. D. Tyrer, "Interferometric fringe analysis using a single phase step technique", *Appl. Opt.* **27**, pp. 4362-4364, 1988
2. D. Colucci, P. Wizinowich, "Millisecond phase acquisition at video rates", *Appl. Opt.* **31**, pp. 5919-5925, 1992
3. M. Kujawińska, D.W. Robinson, "Multichannel phase-stepped holographic interferometry", *Appl. Opt.* **27**, pp. 312-320, 1988
4. D. C. Williams, N. S. Nassar, J. E. Banyard, M. S. Virdee, "Digital phase-step interferometry: a simplified approach", *Opt. Las. Tech.* **23**, pp. 147-150, 1991
5. T. Bothe, J. Burke, H. Helmers, "Spatial phase shifting in ESPI: minimization of phase reconstruction errors", *Appl. Opt.* **36**, pp. 5310-5316, 1997
6. M. Lehmann, "Phase-shifting speckle interferometry with unresolved speckles: a theoretical investigation", *Opt. Comm.* **128**, pp. 325-340, 1996
7. Y. Surrel, "Design of phase-detection algorithms insensitive to bias modulation", *Appl. Opt.* **36**, pp. 805-807, 1997
8. J. Burke, H. Helmers, C. Kunze, V. Wilkens, "Speckle intensity and phase gradients: influence on fringe quality in spatial phase shifting ESPI-systems", *Opt. Comm.* **151**, pp. 144-152, 1998
9. Y. Y. Cheng, J. C. Wyant, "Phase shifter calibration in phase-shifting interferometry", *Appl. Opt.* **24**, pp. 3049-3052, 1985
10. J. A. Leendertz, "Interferometric displacement measurement on scattering surfaces utilising speckle effect", *J. Phys. E: Sci. Instrum.* **3**, pp. 214-218, 1970
11. R. S. Sirohi, J. Burke, H. Helmers, K. Hinsch, "Spatial phase shifting for pure in-plane displacement and displacement-derivative measurements in ESPI", *Appl. Opt.* **36**, pp. 5787-5791, 1997
12. W. H. Press, B. P. Flannery, S. A. Teukolsky, W.T. Vetterling, *Numerical Recipes in C*, p. 305, Cambridge University Press, Cambridge, 1988
13. G. Å. Slettemoen, J. C. Wyant, "Maximal fraction of acceptable measurements in phase-shifting speckle interferometry: a theoretical study", *JOSA A* **3**, pp. 210-214, 1986
14. M. Lehmann, "Optimization of wave intensities in phase-shifting speckle interferometry", *Opt. Comm.* **118**, pp. 199-206, 1995
15. H. A. Vrooman, A. A. de Maas, "Image-processing algorithms for the analysis of phase-shifted speckle interference patterns", *Appl. Opt.* **30**, 1636-1641, 1991
16. J. W. Goodman, "Statistical properties of laser speckle patterns", *Laser speckle and related phenomena*, J. C. Dainty, ed., pp. 38-39, Springer, Berlin, 1975
17. S. Donati and G. Martini, "Speckle-pattern intensity and phase: second-order conditional statistics", *JOSA* **69**, 1690-1694, 1979
18. K. G. Larkin, B. F. Oreb, "Propagation of errors in different phase-shifting algorithms: a special property of the arctangent function", *Interferometry: Techniques and Analysis*, G. M. Brown, O. Y. Kwon, M. Kujawińska, G. T. Reid, Eds., Proc. SPIE Vol. **1755**, pp. 219-227, SPIE, Washington, 1992.
19. N. Shvartsman, I. Freund, "Speckle spots ride phase saddles sidesaddle", *Opt. Comm.* **117**, 228-234, 1995, and references therein
20. K. Freischlad, C. L. Koliopoulos, "Fourier description of digital phase-measuring interferometry", *JOSA A* **7**, 542-551, 1990
21. M. Takeda, H. Ina, S. Kobayashi, "Fourier-transform method of fringe-pattern analysis for computer-based topography and interferometry", *JOSA* **72**, 156-160, 1982
22. A. E. Ennos, "Speckle interferometry", *Laser speckle and related phenomena*, J. C. Dainty, ed., p. 210, Springer, Berlin, 1975